RMetS
Royal Meteorological Society

An analysis of the diurnal cycle of precipitation over Dakar using local rain-gauge data and a general circulation model

Y. Sane,[a] M. Bonazzola,[a]* C. Rio,[a] P. Chambon,[a] T. Fiolleau,[a] I. Musat,[a] F. Hourdin,[a] R. Roca,[a] J.-Y. Grandpeix[a] and A. Diedhiou[b]

[a]*Laboratoire de Météorologie Dynamique du CNRS, IPSL, Paris, France*
[b]*Laboratoire d'Etude des Transferts en Hydrologie et Environnement, IRD, Grenoble, France*

*Correspondence to: M. Bonazzola, LMD, UPMC, 4 place Jussieu, Tour 45-55 BP 99, 75252 Paris Cedex 05, France.
E-mail: mbonaz@lmd.jussieu.fr

The representation of the diurnal cycle of local deep convection in two versions of the Laboratoire de Météorologie Dynamique–Zoom (LMDZ) General Circulation Model is evaluated using rainfall observations of a rain-gauge network in Senegal. An interpretation of the observed rainfall diurnal modes is attempted by partitioning rainfall as a function of rain-rate intensities and the origin, age and size of associated cloud systems. Our analysis shows a complex multipeak diurnal cycle and a large spatial variability over the rain-gauge domain of typically 100 km. Our results are consistent with the picture of a diurnal cycle of high convective rain rates associated with young and small cloud systems generated in the vicinity of the rain gauges, peaking in late afternoon and superimposed with precipitation associated with long propagative mesoscale convective systems or squall lines with no preferential time over the rain-gauge network. It is shown that these local observations of convection and rain can be used to evaluate the representation of the diurnal cycle of precipitation in a general circulation model with a typical horizontal resolution of 100 km. Two versions of the LMDZ model, including different parametrizations of boundary-layer turbulence, convection and clouds, are compared with observations. In the new parametrization, considering the role of boundary-layer thermals in deep convection preconditioning and the role of cold pools in its sustainment allows us realistically to shift the maximum of precipitation and cloud cover to late afternoon.

Key Words: West African monsoon; AMMA campaign; tropical precipitation; mesoscale convective system

Received 15 August 2011; Revised 2 February 2012; Accepted 26 February 2012; Published online in Wiley Online Library

Citation: Sane Y, Bonazzola M, Rio C, Chambon P, Fiolleau T, Musat I, Hourdin F, Roca R, Grandpeix J-Y, Diedhiou A. 2012. An analysis of the diurnal cycle of precipitation over Dakar using local rain-gauge data and a general circulation model. *Q. J. R. Meteorol. Soc.* DOI:10.1002/qj.1932

1. Introduction

The diurnal cycle is one of the most prominent modes of variability of the tropical climate system (Desbois *et al.*, 1988). An accurate simulation of the amplitude and phase of the diurnal cycle in cloudiness and precipitation in the Tropics is important for climate modelling, because of the crucial role of clouds in radiative and water budgets.

Surface observations and satellite measurements have been used for several decades to document the diurnal cycle in rainfall and convective systems. Throughout the global Tropics, the Cloud Archive User Service (CLAUS) window-brightness temperatures and the tropical Rainfall Measuring Mission (TRMM) satellite measurements have demonstrated the existence of primary diurnal modes of convective intensity and rainfall (Yang and Slingo, 2001;

Nesbitt and Zipser, 2003; Yang *et al.*, 2008). Over tropical continents, convection and precipitation maxima are usually found in mid to late afternoon and correspond to the maximum boundary-layer destabilization caused by daytime insolation (Wallace, 1975).

This simple picture has been refined by the detection of secondary diurnal modes at regional and global scales. Yang *et al.* (2008) show in a comprehensive study that the expected primary mode of precipitation over continents is generally accompanied by a secondary maximum occurring in the late evening to early morning. Mohr (2004) confirms that the diurnal cycle of precipitation is bimodal north of 10°N in sub-Saharan Africa. In some cases, the late-evening to early-morning precipitation maximum becomes even stronger than the mid-to-late afternoon peak, as shown by Shinoda *et al.* (1999) over Niamey (Niger) and by Carbone and Tuttle (2008) in the central United States. Yang *et al.* (2008), Shinoda *et al.* (1999), Carbone and Tuttle (2008) and Mohr (2004) all find a high variability of the secondary diurnal mode, depending on the region, season and year.

Several factors are suggested to explain the bimodal nature of the diurnal cycle and its variability. Yang and Smith (2008) interpret the different diurnal modes by partitioning the total rainfall into convective and stratiform components. Mohr (2004) and Mathon and Laurent (2001) find that the variability of the diurnal cycle in sub-Saharan Africa is primarily influenced by variability in the frequency and life cycle of organized convective systems. Laing *et al.* (2008) find that diurnal frequency maxima of convection result from the superposition of local diurnal maxima with the delayed-phase arrival of propagating systems, which control the rainfall peak in some regions (for example over Niger: Shinoda *et al.*, 1999). The importance of propagating systems for the rainfall diurnal cycle was also noticed by Carbone and Tuttle (2008) in the central United States.

The ability of general circulation models (GCMs) to represent this diurnal cycle provides an integrated test for their physical parametrizations, as various elements involving the surface, boundary layer and free atmosphere have to be properly represented to achieve the correct amplitude and phase. On the other hand, the validation of one single parametrization is delicate in this context, as the observed rainfall cycle results from the interaction of several different processes. Most GCMs show discrepancies from observations, as they produce a diurnal cycle of rain in phase with insolation, leading to a maximum around midday instead of late afternoon (Yang and Slingo, 2001).

The present study has three objectives. We first analyse the rainfall diurnal cycle observed by a rain-gauge network in Senegal and highlight its specificity in the West African context. Our second aim is to show that although these observations are local, they can be used to validate the rainfall diurnal cycle of a GCM, provided they are carefully interpreted. Finally, the improvement of the rainfall diurnal cycle in the Laboratoire de Météorologie Dynamique–Zoom (LMDZ) GCM by a new parametrization of deep convection is documented. The validation performed by the rain-gauge network is complemented by a regional comparison of GCM outputs with the TRMM Multisatellite Analysis (TMPA) over the whole of West Africa, which supports our results.

Our validation exercise requires a careful methodology. As the propagation of convective clouds from one grid point to another is currently not included in the LMDZ GCM, the modes of the diurnal cycle associated with propagative systems cannot be represented. To compare similar physical processes in observations and simulations, we then focus on the evaluation of the life cycle of local convective clouds by filtering out propagative systems detected by a tracking technique from observed data. We then analyse the diurnal mode associated with local deep convection, which is directly comparable with the outputs of LMDZ physical parametrizations.

The rain-gauge network and the spatial patterns of the observed rainfall are briefly described in section 2. The characteristics of the diurnal cycle are detailed in section 3, while an interpretation of the detected diurnal modes is discussed in section 4. Section 5 discusses some aspects of the LMDZ GCM validation and conclusions are given in section 6.

2. Rain-gauge data

The present analysis deals with rainfall data of the Dakar rain-gauge network, located in the region of Dakar (Senegal) in the vicinity of the coast (Jenkins *et al.*, 2010). The rain-gauge network (Figure 1) extends from 14.13–15.22°N in latitude and from 16.47–17.47°W in longitude. It is composed of 40 stations; among them 20 stations (stations 1–20) forming a dense network are separated from each other by an average distance of 1.7 km, while 20 other stations (stations 21–40) are separated by an average distance of 18.8 km. Rain gauges of stations 22, 23, 26, 34 and 38 were not operational during the period August–September 2006, and some recording errors occurred for stations 1, 10 and 11 of the dense network. Rainfall is measured each hour during the whole two-month period.

We first consider precipitating events. We define the beginning of a precipitating event measured by a rain gauge as the time when the hourly rain rate at that rain gauge becomes strictly positive, and its end when the hourly rain rate becomes null. The numbers of precipitating events occurring in August–September 2006 are shown on a map in Figure 2 for each station. They comprise between 12 and 50 outside the dense network and between 41 and 56 within the dense network. On average, the dense network stations thus record a higher number of precipitating events (50) than the other stations (30 events per station).

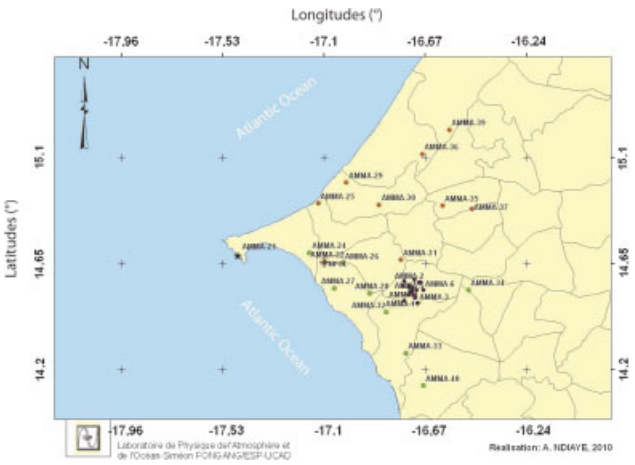

Figure 1. Geographical map showing the rain-gauge network in Senegal. This figure is available in colour online at wileyonlinelibrary.com/journal/qj

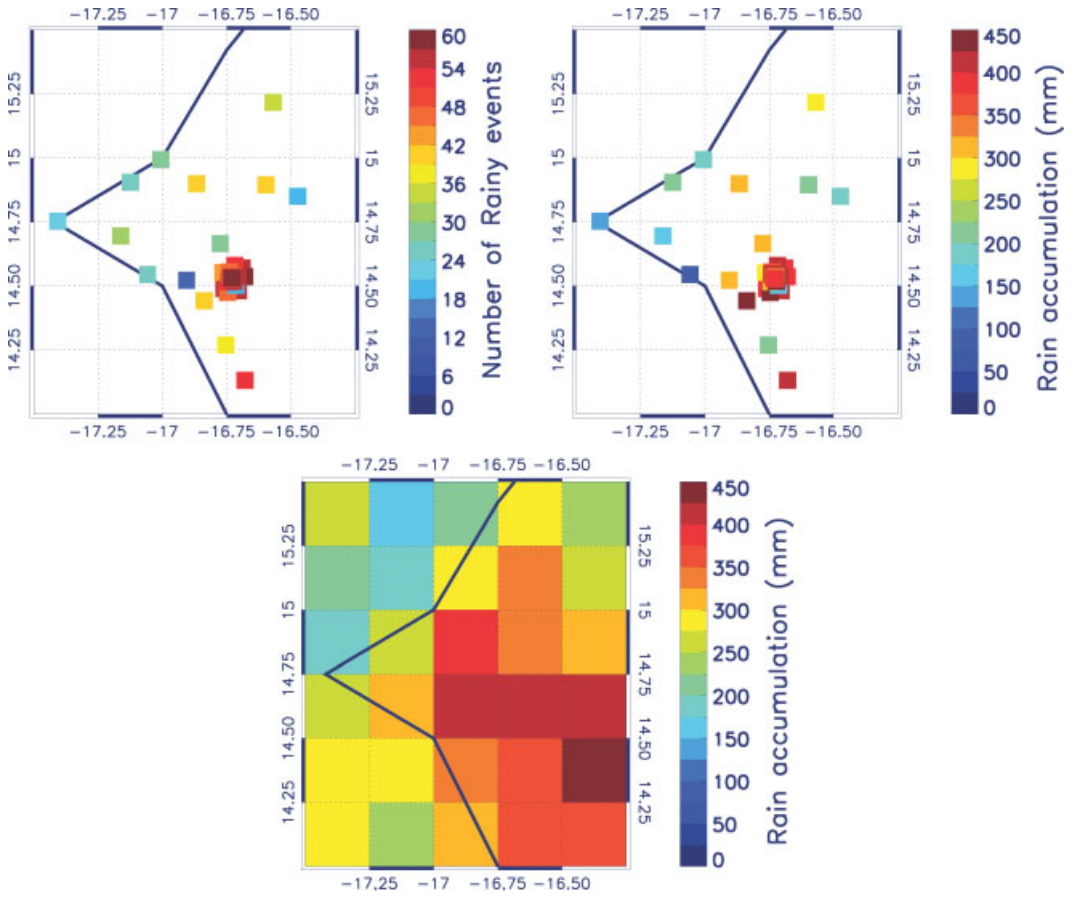

Figure 2. (a) Number of precipitating events in August and September 2006 detected by rain-gauge stations. (b) Cumulated precipitation over the same period detected by rain-gauge stations. (c) TMPA cumulated precipitation over the same period. The same colour convention is chosen for TMPA data and rain gauges.

Table 1. The number of precipitating events per station and the total rainfall per station during August–September 2006, recorded inside and outside the dense network.

	Out of dense network		Dense network	
	Occurrence	Rainfall	Occurrence	Rainfall
Min. value	12	72	41	276
Max. value	50	416	56	415
Mean	30	232	50	361
Std.	10	100	4	44

The cumulated precipitation over the whole period shows similar spatial variations, with more rainfall recorded in the dense network (361 mm per station on average) than outside (232 mm of precipitation per station). Cumulated rainfalls comprise between 72 mm and 416 mm outside the dense network and between 276 mm and 415 mm within the dense network (Figure 2). As expected, the standard deviation of the number of precipitating events and rainfall calculated among the stations is smaller within the dense network than outside (see Table 1). The detected spatial heteorogeneity of rainfall over a network region of a typical scale of 100 km is in good agreement with the study of Chambon *et al.* (2011), who find a correlation length for rainfall of about 50 km over West Africa.

Rain-gauge rainfall is compared in Figure 2 with the TRMM Multisatellite Analysis (TMPA). The TMPA dataset is an operational rainfall-estimation product of the TRMM mission (Huffman *et al.*, 2007), which provides instantaneous rainfall estimates at a resolution of 0.25° and 3 h from 50°N–50°S. These rain estimates are a combination of microwave retrievals of rain rates and, when no microwave observation is available, microwave-calibrated infrared estimates of rain rates. The Global Precipitation Climatology Project monthly rain-gauge analysis is then used for monthly rescaling (Huffman *et al.*, 1997). The microwave retrievals combine observations from multiple satellite passive microwave imagers [Special Sensor Microwave Imager (SSM/I), TRMM Microwave Imager (TMI), Advanced Microwave Scanning Radiometer for Earth Observing System (AMSR-E) and Advanced Microwave Sounding Unit-B (AMSU-B)] converted into rain rates using the Goddard Profiling algorithm (GPROF: Kummerow *et al.*, 2001). The microwave-calibrated infrared estimates combine data from the operational fleet of geostationary meteorological satellites. TMPA was validated over Western Africa with surface-rainfall products and demonstrated good performance at meteorologically relevant scales over this region (Roca *et al.*, 2010).

TMPA data show a pattern consistent with the rain-gauge network, again with a maximum in the region of the dense network. The heterogeneity of the values is higher for rain-gauge data, a result directly attributable to the differences in spatio-temporal resolution between the two datasets. Nevertheless, comparison confirms again the specificity of the dense network region, characterized by higher precipitation.

3. Characteristics of the diurnal cycle of precipitation

To examine which factors control the diurnal cycle of rainfall, we basically follow Nesbitt and Zipser (2003) and Mohr (2004) by considering the number of precipitating events, the percentage of total precipitation and the average cumulated rainfall per precipitating event, occurring in 3 h local time blocks (Figure 3). The same event is counted several times if it is observed by several stations. Thus the same event occurring over the dense network may have a much higher weight than an event occurring over one or a few rain gauges only. To have a correct representation of the diurnal cycles over the dense network and over the entire network, we then process on one hand the dense network data only and on the other hand the data of the entire homogeneous network, where the dense network is represented by one station only, defined as the average of all stations of the dense network.

Over the entire network, the occurrence of precipitating events has a dominant peak at 1500–1700 local time and two secondary peaks located at 0000–0200 and 0900–1100. In terms of rainfall, the secondary peaks represent 14% and 13% of total precipitation respectively, while the dominant peak represents 24% of total rainfall between 1500 and 1700 local time. The average cumulated rainfall per event has similar order of magnitude in all time blocks, except for a minimum between 1200 and 1400.

In the dense network we observe two peaks of occurrence, the 0900–1100 peak being slightly greater than the 1500–1700 peak. However, the 0900–1100 peak only represents 9% of total rainfall, while the mid-afternoon peak represents 26% of total rainfall between 1500 and 1700 and 51% between 1500 and 2000. The average cumulated rainfall per event can reach 13 mm between 1800 and 2000, whereas it does not exceed 9.5 mm outside the dense network. This result confirms the detection of particularly intense systems in the dense network, as found in section 2, and shows that these intense precipitating events preferentially occur in the late afternoon.

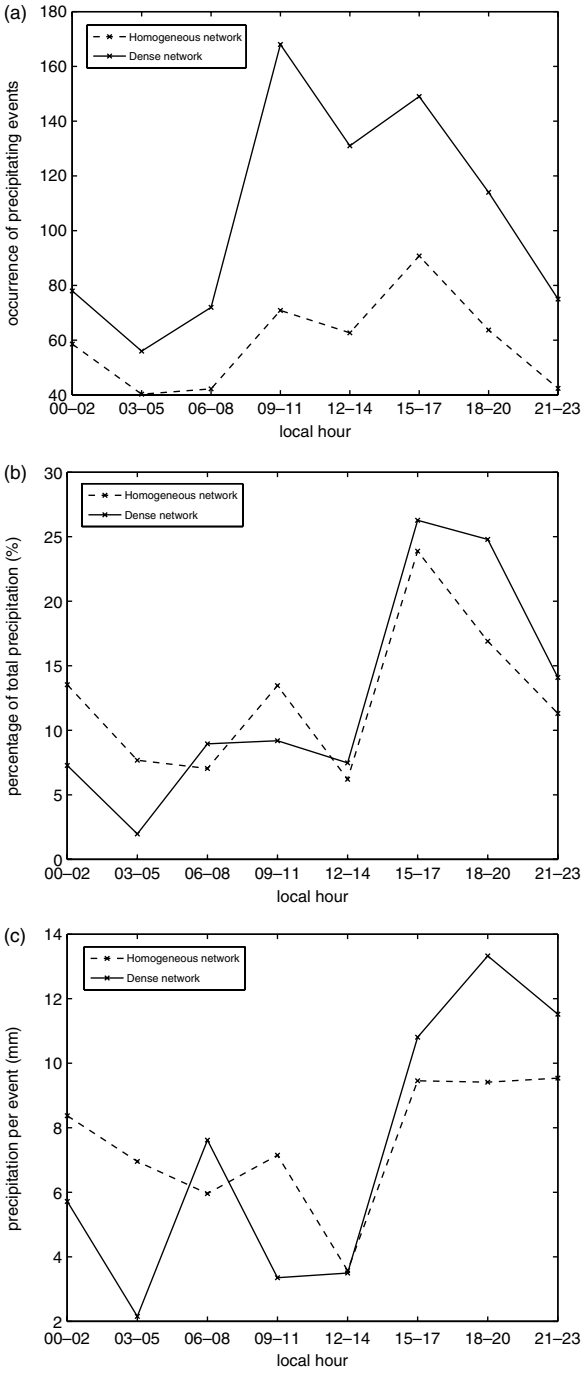

Figure 3. Number of precipitating events, percentage of total precipitation and average cumulated rainfall per precipitating event, occurring in 3 h local time blocks, for the entire homogeneous network (see text) and the dense network only.

4. Diurnal cycle interpretation

4.1. Instantaneous rain rates

A high cumulated rainfall per event can be attributable to particularly long events, or to high instantaneous rain rates. We investigate this point further by analysing the durations of rainfall events and the conditional hourly rain rates directly measured by the rain gauges.

We first plot in Figure 4 the mean durations of rainfall events as a function of the time when they reach their maximal intensities, in 3 h time blocks. Here the durations are measured at the rain-gauge stations, i.e. at fixed locations, and thus do not correspond to the ages of precipitating cloud systems that might propagate. The two diurnal cycles of the event durations, calculated for the dense network and for the entire homogeneous network, do not show any strong peak, all the durations falling between 1.3 and 3.2 h. Thus the high cumulated rainfall per event detected in the late afternoon in the dense network cannot be explained by particularly long rainfall events that would reach their maximal intensities at that time.

In a second step, we study the diurnal cycle of conditional instantaneous rain rates as a function of their intensity. We define a rain-rate threshold and we represent in Figure 5 (top) the occurrences of rain rates below and above that threshold and the sum of these two components as a function of local time, in the dense network (right column) and in the entire homogeneous network (left column), where the stations of the dense network have been replaced by one single typical station.

The use of a single rain-rate threshold does not allow us to distinguish clearly between stratiform and convective rainfall, as low rain rates can have both origins. However, most of the highest instantaneous rain rates are probably attributable to convective systems, as Schumacher and

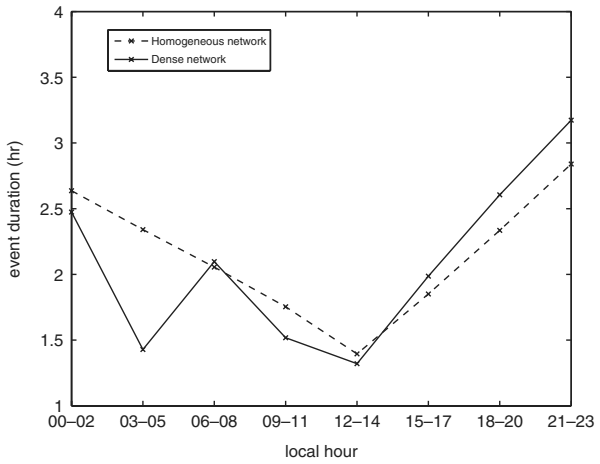

Figure 4. Mean durations of rainfall events as a function of the local time of their maximal intensities, for the entire homogeneous network and the dense network only.

Houze (2003) note that the ratio between convective and stratiform rain rates reaches 10 over continental tropical Africa. We define a threshold of 5 mm h^{-1} as rain rates above that level are generally identified as convective (Schumacher and Houze, 2003).

The solid lines of Figure 5 (top) corresponding to all instantaneous rain rates (lower and greater than 5 mm h^{-1}) slightly differ from the two curves shown in Figure 3 (top) because we now consider the times of occurrence of instantaneous rain rates, whereas we previously recorded the times when rainfall events reach their maximal intensity. Rain rates lower than 5 mm h^{-1} occur much more frequently (at a level of 80%) than rain rates above that threshold. Higher rain rates preferentially occur in the 1500–1700 time block, the peak being more pronounced in the dense network.

Percentages of total precipitation are calculated in each 3 h block in Figure 5 (bottom). Between 0000 and 0200, rain rates higher than 5 mm h^{-1} contribute to total precipitation at levels of 53% and 71% in the dense network and the entire network, respectively. Between 0900 and 1100, the contributions of these rain rates reach 62% and 75%. The 1500–1700 peak is primary controlled by rain rates above 5 mm h^{-1}, especially in the dense network where they represent 91% of total rain rates.

We can then conclude that the particularly high cumulated rainfall per event in the late afternoon in the dense network is attributable to high instantaneous rain rates. Our results are consistent with those found by e.g. Nesbitt and Zipser (2003), who detected a convective intensity peak over land in the late afternoon. Nevertheless we find that typically convective rain rates also contribute significantly to total rainfall during the night and at other times of the day.

4.2. *Characteristics of mesoscale convective systems*

In order to interpret further the diurnal cycle of precipitation, we focus on the cloud systems detected in the region of the rain-gauge network and associated with rain. We use a tracking technique applied to infrared Meteosat Second Generation (MSG) images to retrieve some of their characteristics.

4.2.1. *Cloud-system tracking*

The cloud-system tracking algorithm (full details in Williams and Houze, 1987; Arnaud *et al.*, 1992; Mathon and Laurent, 2001) is composed of two steps: the detection of the cloud system at a given time and the tracking along the time. Meteosat images in the thermal window (10–12 μm) are segmented using a clustering routine that delineates a continuous region in space with brightness temperatures lower than a threshold of 233 K. The minimum size to characterize the cloud system is 5000 km^2. The clusters detected at time $t + 1$ are matched with those of time t, on the basis of a spatial overlap between the two segmented images that must be greater than 10 000 km^2 or greater than 50% of the area of one of the two consecutive clusters. When no overlapping is detected on the image at time $t + 1$, the cloud system is considered as having dissipated. Conversely, the cloud system generates at time $t + 1$ if no overlapping is observed at time t.

4.2.2. *Analysis of precipitating mesoscale convective systems*

Cloud systems are considered as precipitating over the rain-gauge network if two conditions are satisfactory:

(1) the fraction F of the cloud surface (defined by infrared brightness temperature pixels lower than 233 K) that overlaps the rain-gauge network area, over the whole rain-gauge area, must be strictly positive;
(2) at least one of the rain gauges must detect rain at that time.

We compute several parameters for the precipitating systems, among which are the local time and the location of their generation. The location of a system is defined by the centre of mass weighted by the inverse of the brightness temperature of each pixel.

The histogram of the generation times, shown in Figure 6, has a strong peak in the afternoon (between 1200 and 1700). The generation locations, represented on the map of Figure 7, sample a rather large area, between longitudes of 18.3°W and 11.9°E and latitudes of 9°N and 17°N. Among the 35 precipitating MCSs, 30 of them form out of the rain-gauge network. As most of the systems are formed over land, the main cause of their formation might be destabilization of the boundary layer resulting from insolation.

For each system we calculate its surface, propagation distance and propagation time from the location of its generation to the rain-gauge network. We consider the cloud surface at the time when the cloud reaches the rain-gauge network, i.e. when fraction F becomes greater than zero. The propagation time is defined as the time interval between the generation time and the time when F becomes strictly positive. The propagation distance is the distance between the centres of mass of the cloud system at these two times.

Figure 8 shows these three parameters for each detected MCS, as a function of their observation time by the rain-gauge network. The 35 precipitating MCSs propagate over distances extending from 0 to 3345 km, during times between 0 and 57 h, with averages of 479 km and 11 h. Among the 35 MCSs, the youngest ones with a mean age lower than 7 h over the rain-gauge network and the local ones with a mean propagating distance lower than 315 km are shown in the left column, whereas the older, propagating

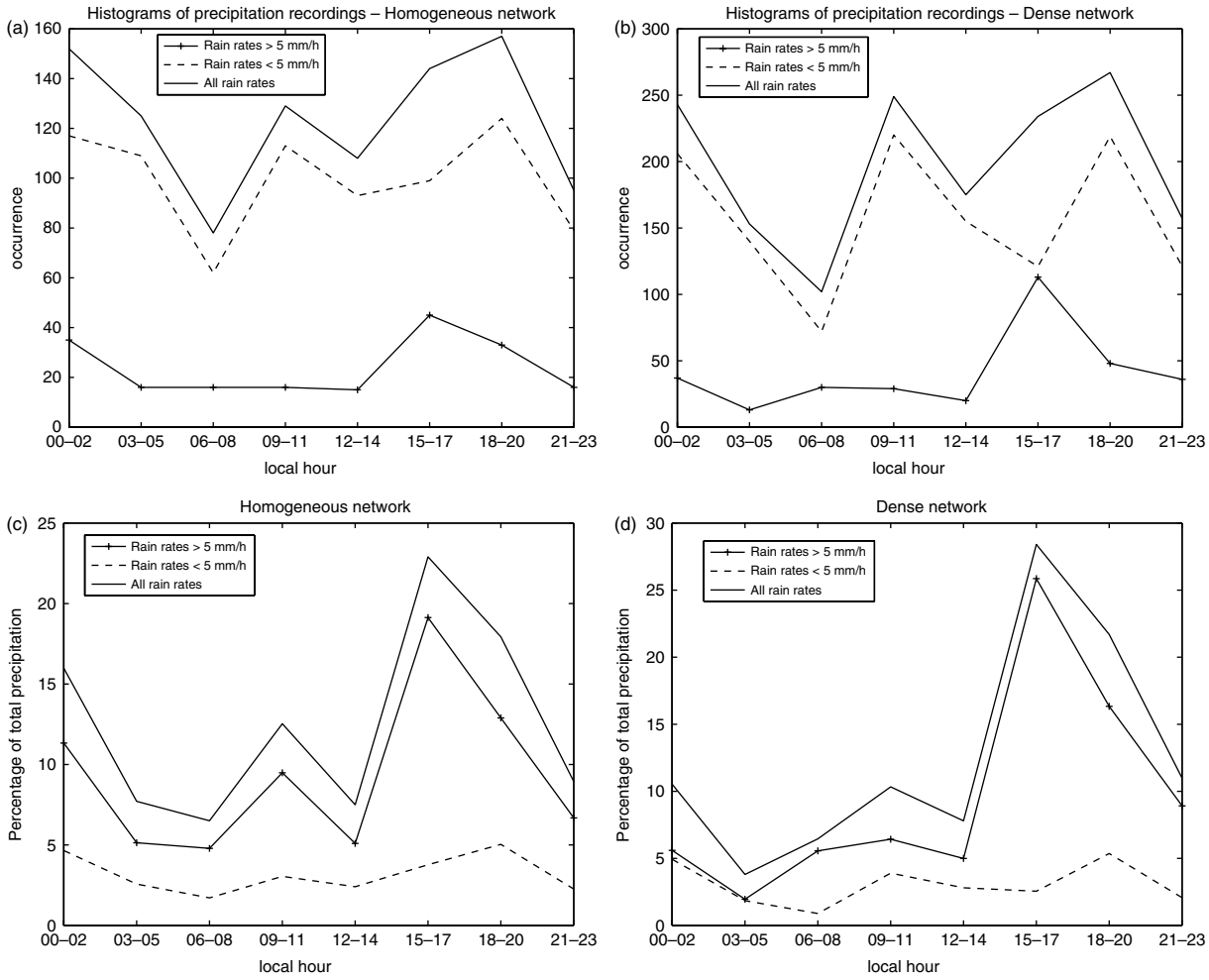

Figure 5. Occurrences of instantaneous rain rates (upper row) and percentages of precipitation (lower row) as a function of local time, in the entire homogeneous network (left column) and the dense network (right column), for all instantaneous rain rates and for rain rates lower and greater than 5 mm h^{-1}.

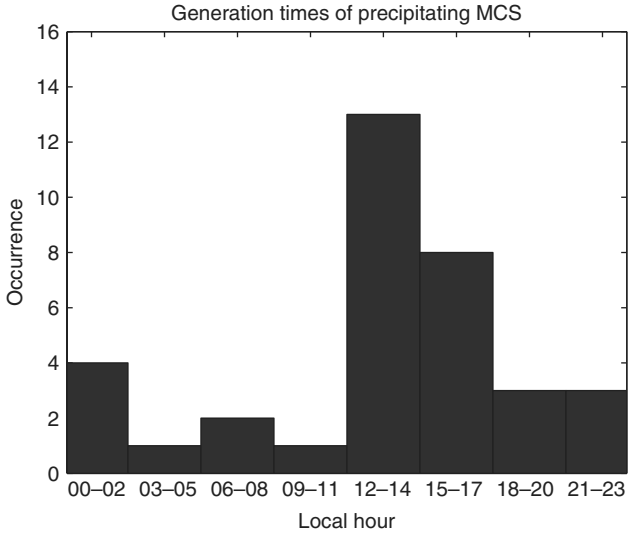

Figure 6. Histogram of the local times of generation of the precipitating MCSs detected over the rain-gauge network in August–September 2006.

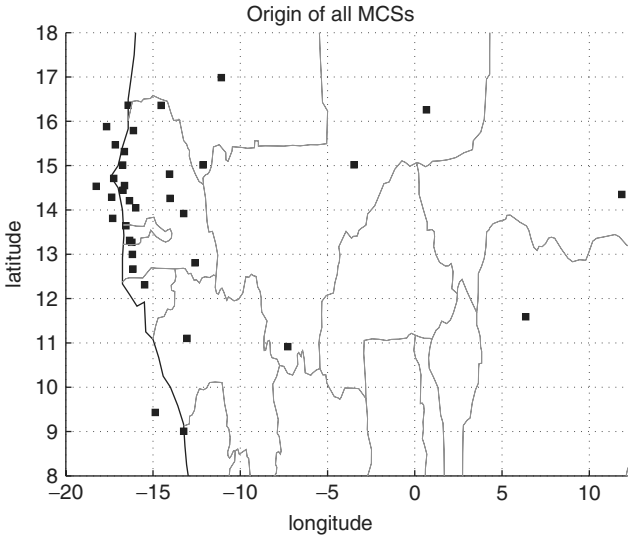

Figure 7. Generation locations of the precipitating MCSs detected over the rain-gauge network in August–September 2006.

ones are represented in the right column. We choose the threshold of 315 km to distinguish between local and non-local cloud systems, as this length is the square root of their mean surface (1.0065×10^5 km^2). A cloud is then considered as non-local if its displacement is larger than its typical length. We set the age threshold equal to 7 h, as a cloud propagates over 315 km in about 7 h, its mean velocity being 45 km h^{-1}. The age and the propagating distance of a

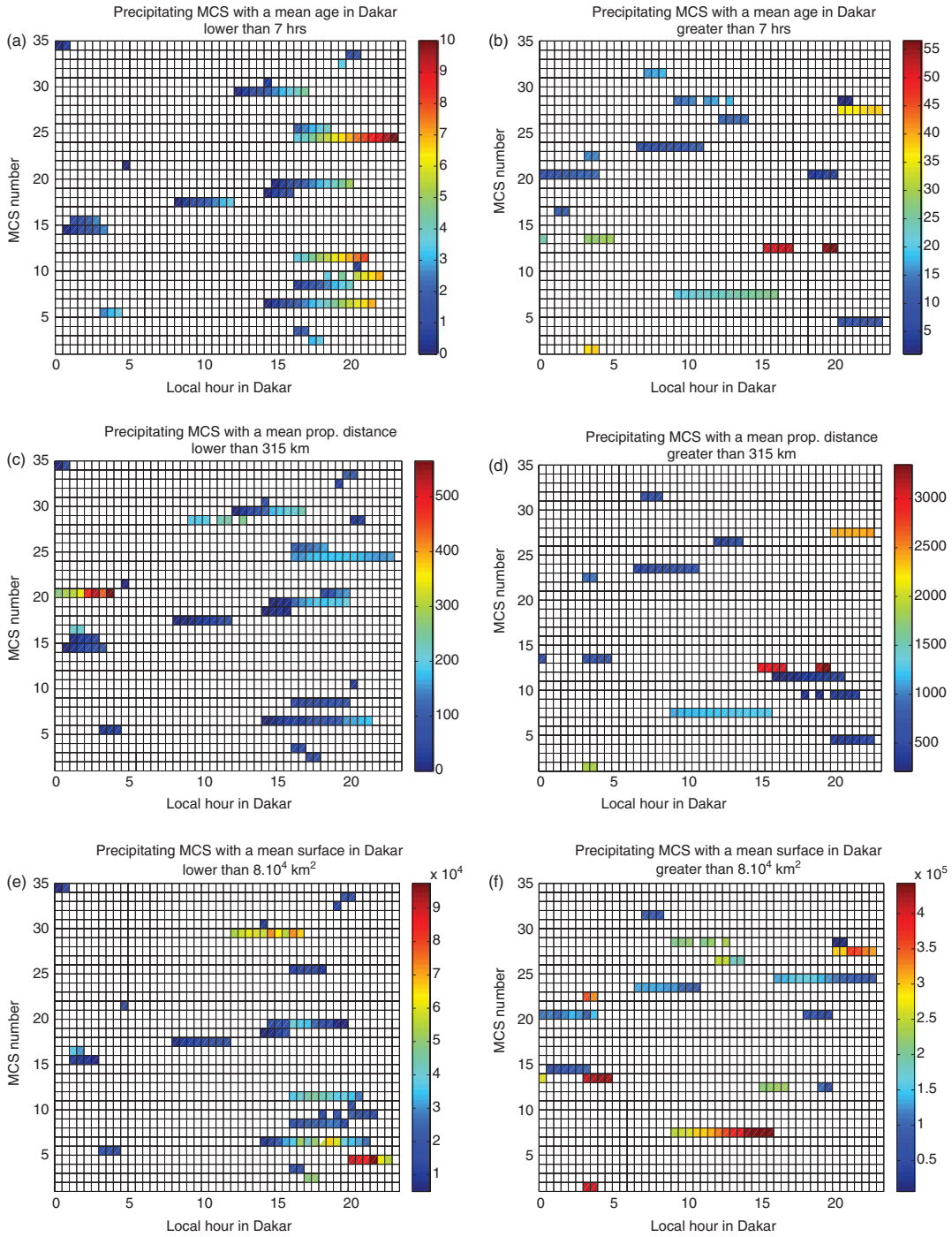

Figure 8. Ages (h), propagation distances (km) and surfaces (km^2) of the precipitating MCSs detected over the rain-gauge network in August–September 2006, as a function of their precipitation time.

given MCS change with time as the cloud moves through the rain-gauge area, this evolution being represented by a colour variation along a given row. Some MCSs–for example MCS 9–appear as intermittent events, because they get out and into the rain-gauge area several times along their trajectories or because precipitation is not registered during the whole passage of the MCS within the rain-gauge region.

Figure 8 shows that a very high proportion (65%) of the youngest MCSs with ages lower than 7 h precipitate between 1500 and 2000, whereas only 23% of older MCSs are found in that time block. Similar behaviour is observed for the propagation distances, 55% of the clouds having propagated less than 315 km before reaching Dakar precipitate between 1500 and 2000 against only 33% for those having propagated over longer distances. Thus the MCSs that are generated locally are more likely to precipitate in the late afternoon, because cloud systems are generally formed at that time or a few hours before.

The surfaces of the MCSs precipitating over Dakar comprise between 5006 and 442 800 km^2 (note again that only cloud systems larger than 5000 km^2 are detected by the tracking algorithm). The smallest MCSs with mean surfaces lower than 8×10^4 km^2 over the rain-gauge network are shown in the left column of Figure 8 (lower), whereas the larger MCSs appear in the right column. Not surprisingly, small MCSs are observed more predominantly in the late

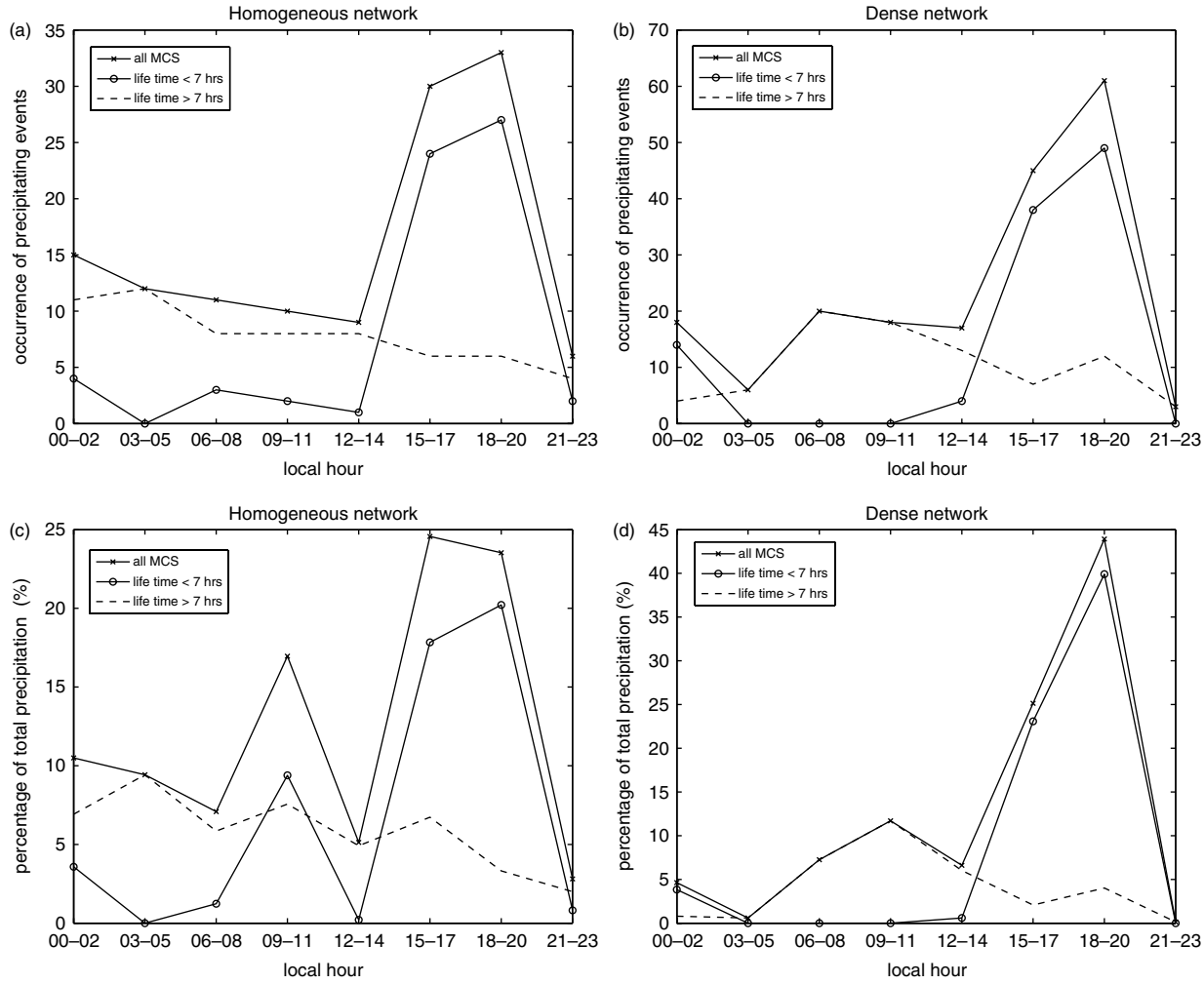

Figure 9. Upper row: Number of precipitating events associated with the MCSs detected by the cloud-tracking algorithm (see text) and occurring in 3 h time-blocks. Lower row: Percentage of total precipitation associated with the detected MCSs in 3 h time-blocks for the entire homogeneous network (left) and the dense network (right), for all MCSs and for MCS ages lower and higher than 7 h.

afternoon than at other times, because of their lower age (60% of clouds smaller than 80 000 km^2 are found in the 1500–2000 time-block, whereas only 29% of larger clouds are observed at these times).

All these results are consistent with the picture of a diurnal cycle of local convection peaking in late afternoon and superimposed with long propagating MCSs or squall lines with no preferential time for precipitation over the rain-gauge region. This property of propagating MCSs is typical of the region of Dakar. In contrast, the propagating events passing through the radar area of Niamey arrive there at a consistent time of the day, between 1500 and 1700 local time (UTC) (Rickenbach *et al.*, 2009), because the majority of the squall lines observed in Niamey originated in the late afternoon of the previous day in a confined elevated region between the longitudes of Niamey (13.3°N, 2.6°E) and Lake Chad (13°N, 14°E) (Rickenbach *et al.*, 2009). The propagating systems observed by the rain gauges in Dakar are also formed at a preferential time in the afternoon (see Figure 6), but their generation locations are much more dispersed (see Figure 7) and so are their propagating times (the maximum propagating time reaches 57 h and the standard deviation of the ages of the systems having propagated more than 315 km is 14 h).

4.2.3. *Diurnal cycle of rainfall associated with MCS*

We study the diurnal cycle of the precipitating events recorded by the rain-gauge network and which are associated with cloud systems detected by the tracking algorithm (*i.e.* with a brightness temperature lower than 233 K and a surface greater than 5000 km^2). The occurrences of the totality of these precipitating events and their contribution to total precipitation, recorded by dense network stations only (right column) and by stations of the entire homogeneous network (left column), are represented by crosses as a function of local time in Figures 9 and 10.

These curves show differences from Figure 3, as the latter includes the precipitating events associated with clouds smaller than 5000 km^2 or warmer than 233 K. For the 0900–1100 time period the occurrence is now much reduced while the percentage of precipitation is not. The large number of events shown in Figure 3 at that time therefore comes from low or small clouds, while the cumulated rainfall essentially comes from a small number of MCSs.

Between the MCS precipitating events, we distinguish those that are associated with cloud systems having an age shorter or longer than 7 h, propagation distances shorter or longer than 315 km and surfaces lower or greater than 8×10^4 km^2. Their occurrence and contribution to total

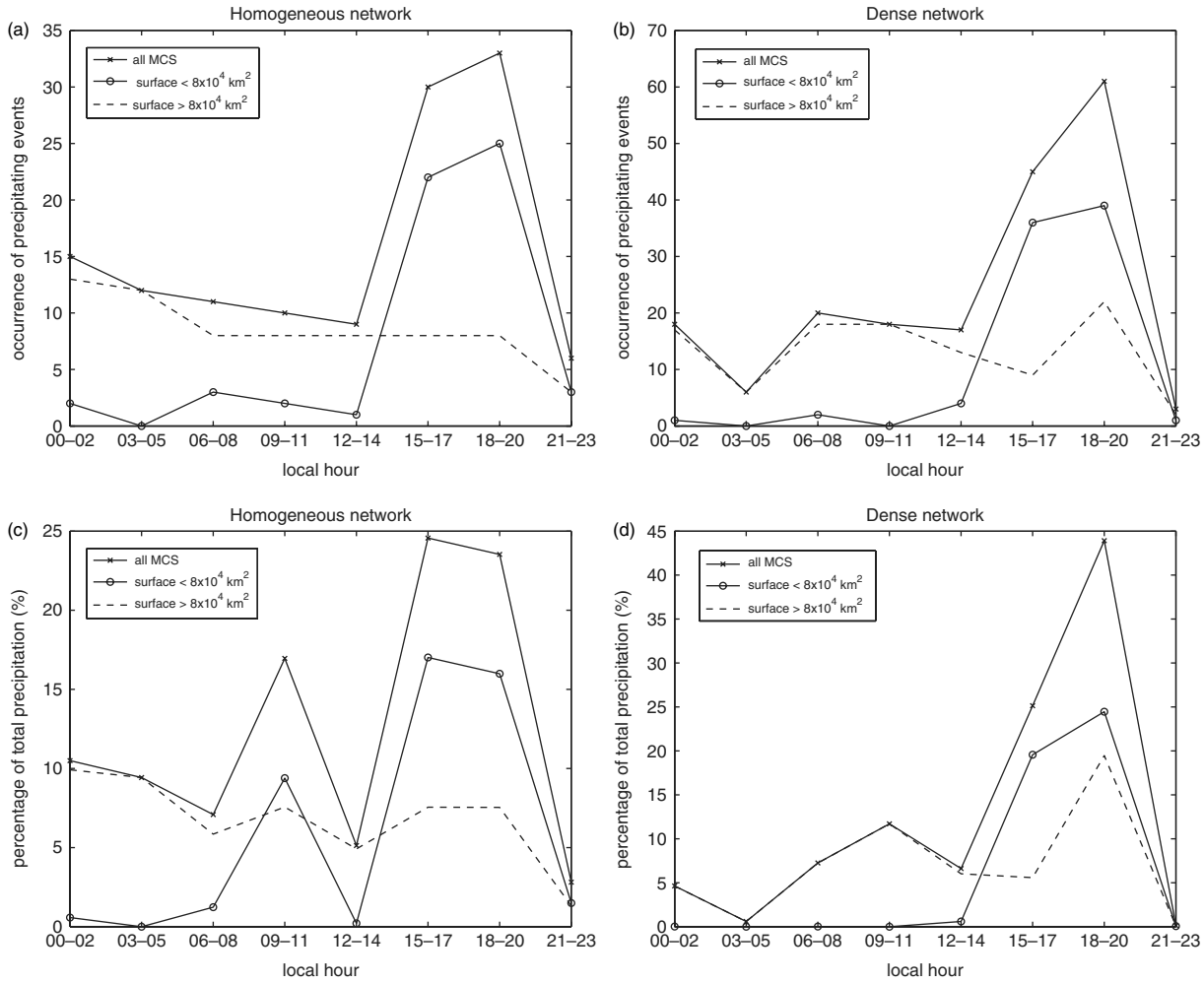

Figure 10. Upper row: Number of precipitating events associated with the MCSs detected by the cloud-tracking algorithm (see text) and occurring in 3 h time-blocks. Lower row: Percentage of total precipitation associated with the detected MCSs in 3 h time-blocks for the entire homogeneous network (left) and the dense network (right), for all MCSs and for MCSs smaller or greater than 8×10^4 km^2.

precipitation are represented as a function of local time in Figures 9 and 10. Figures corresponding to the thresholds of 7 h and 315 km are very similar, therefore only the former is shown (Figure 9). As previously noted, the older MCSs, as well as the larger ones and those having propagated long distances, do not precipitate in any preferential time block, whereas the younger, smaller and local MCSs mostly precipitate between 1500 and 2000.

More precisely, MCSs having an age lower than 7 h explain 79% of the precipitation recorded by the rain gauges of the entire homogeneous network between 1500 and 2000, versus 21% for older MCSs (Figure 9). In the same time block, local cloud systems having propagated less than 315 km contribute to precipitation at a level of 75%, versus 25% for propagative systems (not shown). Results are even more pronounced in the dense network, where young and local MCSs respectively contribute at levels of 91% and 95% to the rainfall occurring between 1500 and 2000. MCSs with a surface lower than 8×10^4 km^2 explain 69% (64%) of the precipitation in the 1500–2000 time block in the entire homogeneous network (dense network); the contribution of smaller clouds is always dominant but becomes weaker between 1800 and 2000 (Figure 10). In the 0900–1100 time-block, results depend on the network considered. In the dense network, precipitation is completely controlled by cloud systems of ages longer than 7 hours, surfaces greater than 8.10^4 km^2 and propagation distances greater than 315 km. However in the entire network, although the occurrence of precipitating events associated with these cloud systems is largest, the amount of rainfall is slightly dominated by younger, smaller and more local MCSs.

In the 0000–0200 time block, precipitation is controlled by large cloud systems of surfaces greater than 8×10^4 km^2 in both the dense network and the homogeneous network. Younger and local MCSs are mostly responsible for rainfall in the dense network, whereas older and propagative systems have the largest rainfall contribution over the entire homogeneous network.

5. Evaluation of the simulated diurnal cycle

In spite of the complexity of the diurnal signal of rainfall in the Dakar region, the above analysis is consistent with the results of e.g. Nesbitt and Zipser (2003), as it shows that over land the precipitation maximum associated with local deep convection mostly occurs in mid to late afternoon. However, most GCMs are known to reproduce a diurnal cycle of continental thunderstorms in phase with insolation (Betts and Jakob, 2002; Guichard *et al.*, 2004) and thus simulate the peak of convective precipitation too early in the day (Yang and Slingo, 2001). Recently, very promising results have been obtained by Rio *et al.* (2009), who could

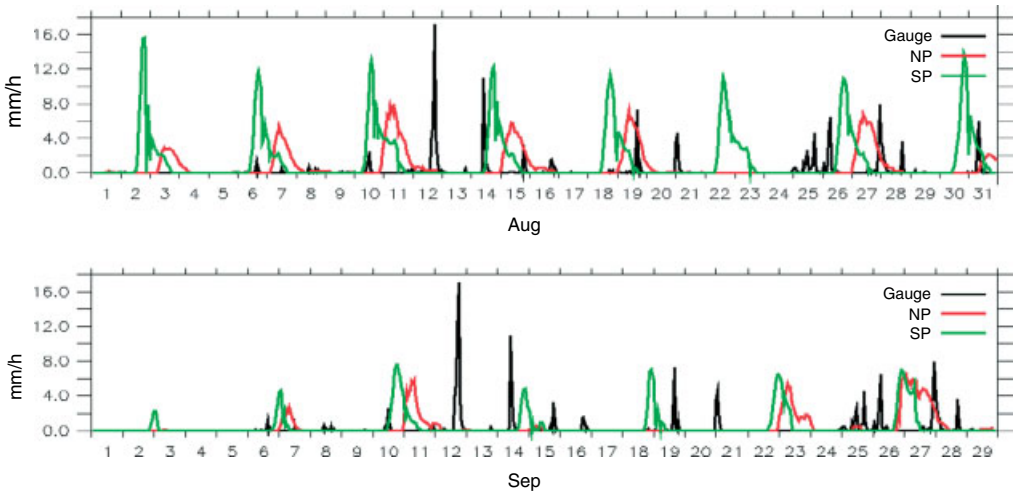

Figure 11. Simulated and observed precipitation as a function of time over the rain-gauge network.

delay rainfall maximum from midday to late afternoon by using in a single-column version of the LMDZ GCM a new package of parametrizations of convection, boundary-layer turbulence and associated clouds. This section is dedicated to the validation of these parametrizations in 3D mode, by comparison of the simulated and observed rainfall diurnal cycles in the region of Dakar.

5.1. *LMDZ GCM simulations*

Simulations are performed using the most recent version LMDZ5 of the global climate model of the Laboratoire de Météorologie Dynamique (Hourdin *et al.*, 2006), recently involved in the Intergovernmental Panel on Climate Change (IPCC) exercise (Dufresne *et al.*, 2005). Its zooming capability allows us to focus the horizontal grid over West Africa and to reach a resolution of 0.7° longitude by 0.6° latitude in the region 25°W–25°E, 5°S–20°N. The LMDZ GCM is integrated for two months with a 39-level vertical resolution, forced by European Centre for Medium-Range Weather Forecasts (ECMWF) ERA-Interim sea-surface temperatures (SSTs) of August and September 2006 and regularly relaxed towards ECMWF ERA-Interim wind reanalyses of the same period with a relaxation time of 3 h (Coindreau *et al.*, 2007). One-hourly diagnostics of convection and precipitation are analysed.

The two simulations use either the standard version of the model physics (SP) or a physical package including new parametrizations of boundary layer, convection and clouds (NP), described in section 5.2. The time evolution of total precipitation as simulated by the two versions of the model is displayed in Figure 11 and compared with observations. In both simulations, we consider the rainfall occurring at the nearest grid point of the rain-gauge network (17°W; 14.5°N). The differences in phase and intensity of precipitation between the two simulations illustrate the effect of the new parametrizations. Differences also appear between observations and simulations. Indeed, even if wind fields are nudged to avoid long-term divergence of model results, it is unlikely that such a model is able to simulate each observed convective system at the right place and time. To do so, the ECMWF reanalyses used to constrain large-scale conditions would need to be perfectly accurate and the spin-up of the LMDZ GCM reduced. Nevertheless, the frequency, intensity and diurnal cycle of convective systems are expected to be correctly represented in a statistical way over a two-month period. This evaluation is presented in section 5.3.

5.2. *Parametrizations of key processes of the life cycle of convective systems*

Most parametrizations for general circulation models aim to represent boundary-layer turbulence as diffusion and deep convection as narrow updraughts compensated by downdraughts and a slower subsidence via the mass-flux approach. However, observational studies have highlighted key processes for the life cycle of convection and clouds that were generally not (or not well enough) represented in climate models. This is the case for boundary-layer thermals, at the top of which cumulus clouds form (Lemone, 1973). Thermals initiate in the unstable surface layer, rise through the entire mixed layer due to buoyancy and overshoot in the inversion layer that progressively cools and moistens, leading to shallow cumulus clouds that pre-condition deeper convection. This is also the case for cold pools that form under convective systems. They are sustained by the evaporation of precipitation within convective downdraughts and spread at low levels. On one hand, they suppress low cumulus clouds by stabilizing the boundary layer. On the other hand, their leading edges uplift the air in front of them, initiating new convection, as shown by observations (Lima and Wilson, 2008) and cloud-resolving modelling (Khairoutdinov and Randall, 2006).

The NP version of LMDZ differs from the previous SP version by the inclusion of specific parametrizations of those two processes: thermal plumes and cold pools. In the SP version, vertical turbulent transport within the boundary layer is treated as diffusion using the Louis (1979) scheme. Deep convection is represented by a mass-flux scheme adapted from Emanuel (1991). In the NP simulation, multiscale processes of the boundary layer are represented by a combination of the same diffusive approach for small-scale turbulence based on Yamada (1983) with a mass-flux scheme for the vertical transport by thermal cells within the convective boundary layer (Rio and Hourdin, 2008). The NP simulation also includes the cold pool parametrization of Grandpeix and Lafore (2010). Another fundamental

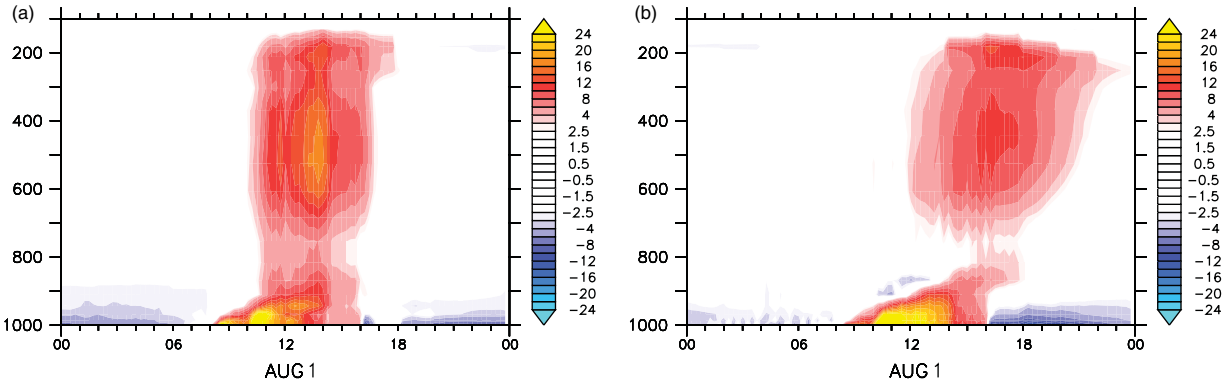

Figure 12. Simulations of the mean diurnal cycle over August and September 2006. Apparent heat source Q_1 (K day^{-1}) obtained with (a) SP and (b) NP versions of LMDZ.

difference between SP and NP is the closure and triggering of convection. While deep convection is controlled by mean environmental variables in the SP simulation, it depends on thermals and cold pools in the NP simulation. Convection is triggered when either thermals or cold pools provide enough lifting energy to overcome convective inhibition. The flux of energy available at cloud base provided by both thermals and cold pools, called the available lifting power, is then used to determine the convective intensity (see Rio *et al.*, 2009 for further details). In both simulations, large-scale condensation and evaporation are handled following Sundqvist (1978) using the Bony and Emanuel (2001) cloud scheme to diagnose cloud cover and liquid water. Regarding radiation, both physical packages include the schemes of Fouquart and Bonnel (1980) for the solar part and Morcrette *et al.* (1986) for the infrared part.

As an illustration of the impact of the new parametrization on the diurnal cycle of convection, we show in Figure 12 the evolution of the heating rate by convection and boundary-layer parametrizations for a column of the model located at 17°W, 14.5°N. In simulation NP, the boundary layer grows deeper with stronger heating of the mixed layer and cooling (associated with a moistening, not shown here) at its top related to overshooting thermals. This vertical transport within thermals is compensated by a slow subsidence within the environment, which brings warm and dry air from the free troposphere to the surface, resulting in a stronger warming and drying of the surface from 0800–1700 in simulation NP compared with SP. The convective inhibition is then higher in NP, which helps to delay the onset of deep convection by several hours. Once deep convection has started, the evaporation of precipitation in the subcloud layer leads to the formation of cold pools at low levels in simulation NP. This corresponds to the low-level cooling seen in the right panel of Figure 12 after 1600. The Figure also shows that convection is maintained by cold pools up to midnight in simulation NP, while it stops at 1800 in SP. The heating rates are quite comparable to those simulated with the same versions of LMDZ for a case of midlatitude continental deep convection as presented in Rio *et al.* (2009), where they were evaluated against a cloud-resolving simulation.

5.3. Characteristics of the simulated diurnal cycle of precipitation

One main goal of the present study is to use rain-gauge observations to assess the representation of the rainfall diurnal cycle in the NP version of the model. We follow the same methodology as in section 3, applied to both simulations. We analyse precipitating events, starting when the hourly rain rate becomes strictly positive and finishing when it becomes null. In the LMDZ GCM, stratiform and convective rainfall components are available at each hour; we thus distinguish between convective and large-scale precipitating events. We plot in Figure 13 the number of these events, the proportion of convective and large-scale precipitation to total precipitation and the mean cumulated rainfalls per precipitating event, occurring in 3 h time blocks. Although Figure 13 is not quantitatively comparable with Figure 3 because of differences in spatial resolution, the peaks times are useful to examine for evaluation of the simulated diurnal cycle.

In the SP simulation, large-scale precipitating events mostly occur between 0900 and 1100; convective precipitating events show a dominant peak at 1200–1700. In the NP simulation, large-scale events are more numerous, as they extend over the night whereas convective events become less frequent, with a maximum of occurrence shifted later in the afternoon between 1500 and 2000. The distribution over the day of all precipitating events in the NP simulation is very similar to the one given by the rain-gauge data (see Figure 3).

In terms of rainfall, convective precipitation is greatly dominant in both simulations. Cumulated over the whole two-month period, convective precipitation reaches 99% and 93% of total rainfall in the SP and NP simulations, respectively. In the SP simulation, the maximum of convective precipitation is found at 1200–1400, with a contribution of 64% in this time block to total precipitation. In the NP simulation, the highest contribution to total rainfall (57%) is found later between 1500 and 1700.

The cumulated rainfalls per event are slightly higher in the NP simulation. The mean large-scale rainfall per event slightly increases in the NP simulation but remains lower than 2 mm at any time. The mean convective rainfall per event also slightly increases in the NP simulation and its maximum of 36 mm is found at 1500–1700, whereas it was located a few hours earlier in the SP simulation.

The significance of the results is checked by extending the comparison of the SP and NP simulations to the whole West African region. We choose as a reference the TMPA data in the domain 25°W–45°E, 10°S–22°N. For each pixel or each model mesh, we construct a histogram of the local times for those precipitating events occurring during the two months.

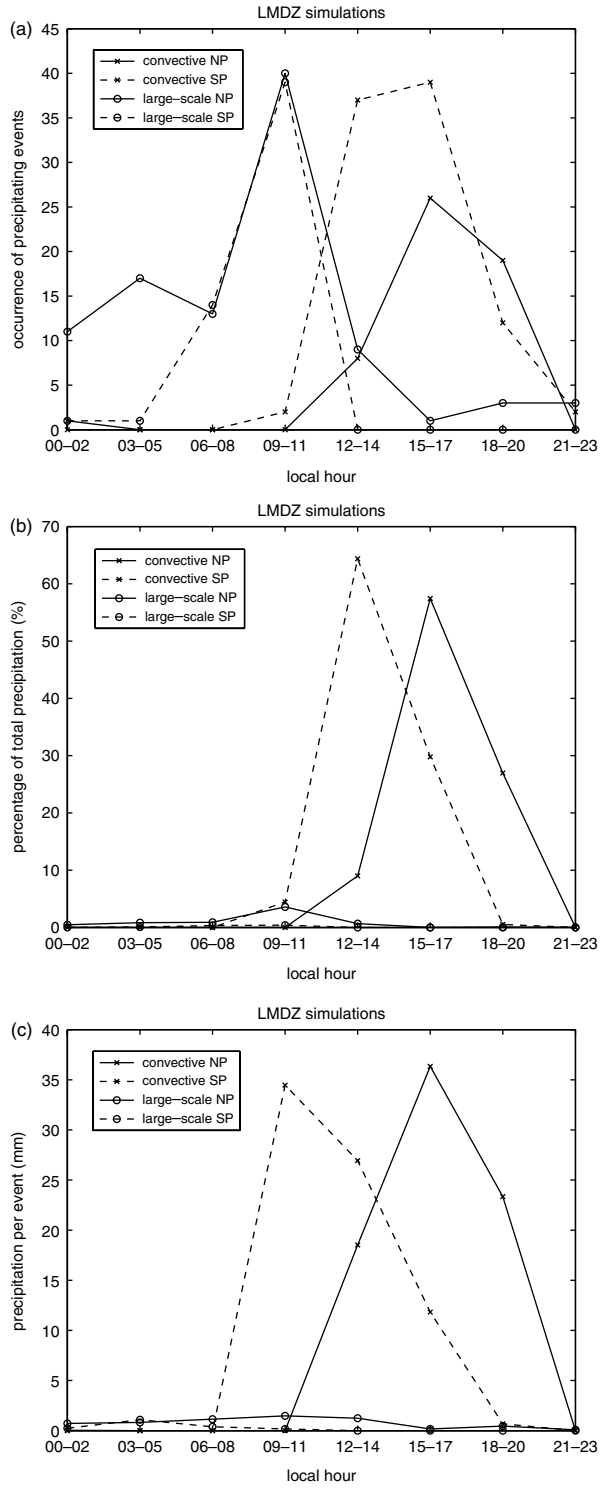

Figure 13. Number of convective and large-scale precipitating events, percentage of convective and large-scale precipitation and average of convective and large-scale rainfall per precipitating event, occurring in 3 h local time blocks, for the SP and NP LMDZ simulations.

In Figure 14, we show a map of the most probable local times for TMPA data and both simulations. Comparison is again limited by the different spatio-temporal resolutions of observations and simulations. However we find in all datasets the same behaviour over ocean, with most probable local times for precipitating events peaking during the night or the early morning.

Over Senegal and Mali (between longitudes 15°W and 0), TMPA data show homogeneous local times between 1600 and 1800, suggesting that the rainfall diurnal cycle is dominated there by locally generated cloud systems. In that region, local times are found between 1200 and 1600 in the SP simulation and between 1400 and 1800 in the NP simulation. The realistic shift towards the late afternoon obtained in 3D mode with the new package of parametrizations thus confirms at a regional scale the results of Rio *et al.* (2009) in 1D mode.

More heterogeneity appears in TMPA data east of longitude 0. For example, in the vicinity of Niamey (13.31°N), local times evolve from the beginning of the night (2200–2400 at 6°E) to the end of the night (0600-0800 in Niamey at 2.6°E) while going westward. This indicates that the time of arrival of propagating MCSs dominates the diurnal rainfall signal in the region of Niamey, as noticed by Rickenbach *et al.* (2009) and Shinoda *et al.* (1999). Not surprisingly, in that region both simulations fail at representing the most probable times of precipitating events, because propagating systems are not represented in the LMDZ GCM.

6. Conclusions

The above analysis of rainfall over Dakar shows a complex multipeak diurnal cycle and a large spatial variability even over the small domain of the rain-gauge network. An interpretation of the different diurnal modes is attempted by partitioning rainfall as a function of rain-rate intensities and the origin, age and size of associated cloud systems.

The analysis shows the following:

- The 0000-0200 peak of precipitation is characterized by large cloud systems (larger than 8×10^4 km^2) and instantaneous rain rates of mixed intensities.
- The 0900–1100 peak corresponds to clouds of mixed characteristics: small isolated and/or warm clouds and MCSs. The MCSs are less numerous but dominant in terms of rainfall. They are mostly large, older than 7 h and propagative, but the younger, more local and smaller ones can give slightly more rain over the entire network.
- The afternoon peak is mostly attributable to young and small clouds generated in the vicinity of the rain-gauge network and associated with high rain rates that are generally convective. The contribution of larger clouds increases in the late afternoon.

Our results are then broadly consistent with the findings of Mohr (2004), who associated the 1400–1800 precipitation peak with young and mature convective systems, the 0200–0600 peak with decaying and stratiform clouds and the 1800–2200 peak with organized convective systems.

It would be too restrictive to point out only one partitioning for interpreting the different peaks of the diurnal cycle, as the different criteria that we used–rain-rate intensity, origin, age and size of cloud systems–might not be decorrelated from each other. Indeed, Houze (1997) notes that 'stratiform rainfall at lower latitudes represents convection at the end of its precipitating life cycle'. Carbone *et al.* (2002) show that 'episodes' resulting from organized convection such as squall lines or MCSs are likely to propagate long distances. Hence, partitioning precipitation as a function of the intensity of instantaneous rain rates might not, in fact, be radically different from classifying convective systems as a function of their age and degree of organization, and the degree of organization

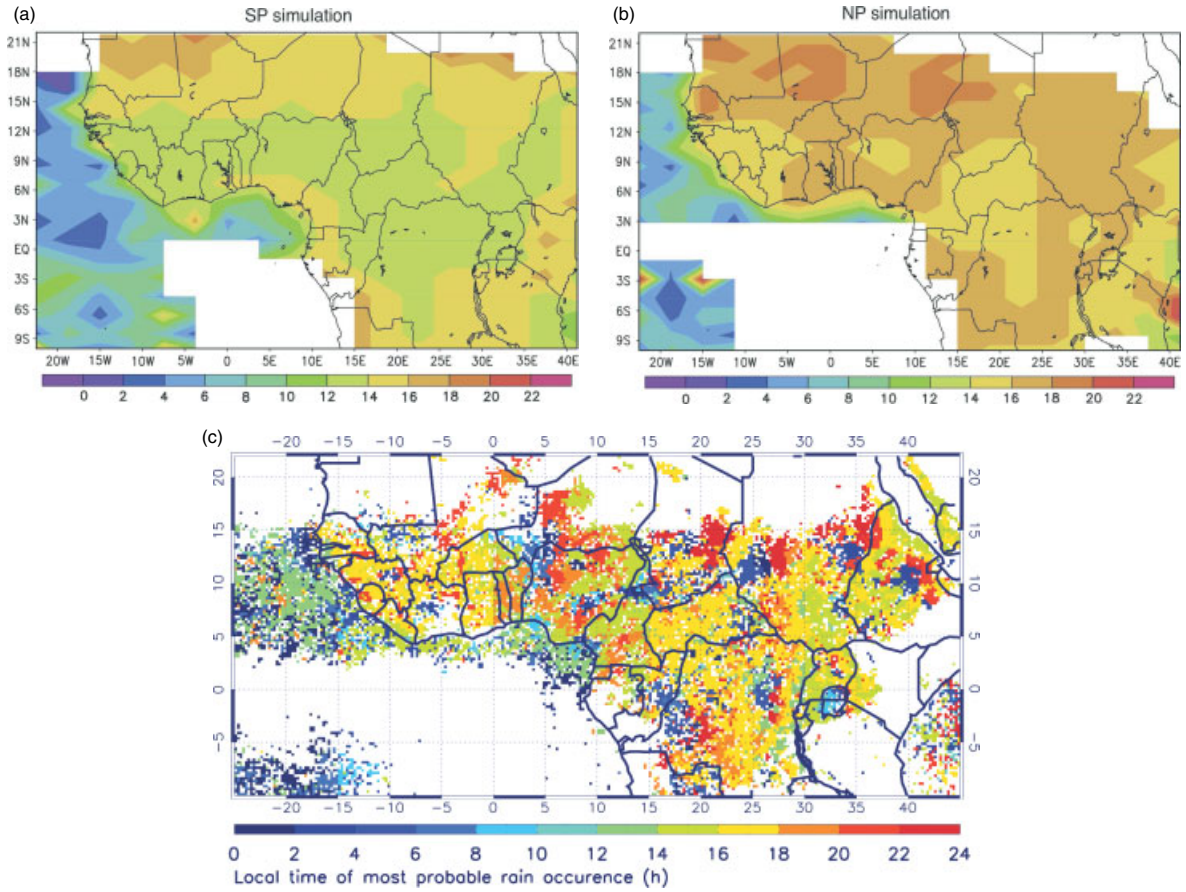

Figure 14. Most probable local times of precipitating events for (a) SP and (b) NP LMDZ simulations and (c) TMPA data.

might, in turn, be linked to the propagation characteristics of the systems.

This study is typical of the comparison made possible today between a model parametrization containing relevant physics and *in situ* observations. Providing a careful analysis, rain-gauge observations can be directly compared with the rainfall produced by a climate model. The new parametrization of Rio *et al.* (2009) used in the 3D mode LMDZ GCM successfully reproduces the convective rainfall peak over land. Considering the role of boundary-layer thermals in deep convection preconditioning and the role of cold pools in its sustainment helps in capturing the observed maximum of precipitation. The obtained shift of cloud cover from midday to late afternoon may have a large impact on climate, as it can modulate the radiative forcing.

The prolongation of deep convection later in the day can also potentially lead to a better representation of the associated anvil clouds and stratiform precipitation if processes leading to their formation are accurately taken into account by either deep convection or the large-scale cloud scheme, given the horizontal resolution used here. The next step in this work is to include the propagation from one grid point to another of squall lines associated with subgrid-scale cold pools, as it could greatly improve the representation of secondary peaks of rainfall occurring over night or in the morning.

Acknowledgement

The numerical simulations presented here were performed on the NEC-SX5 of the IDRIS/CNRS computer centre.

References

Arnaud Y, Desbois M, Maizi J. 1992. Automatic tracking and characterization of African convective systems on Meteosat pictures. *J. Appl. Meteorol.* **31**: 443–453.

Betts AK, Jakob C. 2002. Study of diurnal cycle of convective precipitation over Amazonia using a single column model. *J. Geophys. Res.* **107**: D4732, DOI: 10.1029/2002JD002264.

Bony S, Emanuel KA. 2001. A parameterization of the cloudiness associated with cumulus convection; evaluation using TOGA COARE data. *J. Atmos. Sci.* **58**: 3158–3183.

Carbone RE, Tuttle JD. 2008. Rainfall occurrence in the US warm season: The diurnal cycle. *J. Climate* **21**: 4132–4146.

Carbone RE, Tuttle JD, Ahijevych D, Trier SB. 2002. Inferences of predictability associated with warm season precipitation episodes. *J. Atmos. Sci.* **59**: 2033–2056.

Chambon P, Jobard I, Roca R, Viltard N. 2012. An investigation of the error budget of tropical rainfall accumulation derived from merged passive microwave and infrared satellite measurements. *Q. J. R. Meteorol. Soc.* DOI: 10.1002/qj.1907.

Coindreau O, Hourdin F, Haeffelin M, Mathieu A, Rio C. 2007. Assessment of physical parameterizations using a global climate model with stretchable grid and nudging. *Mon. Weather Rev.* **135**: 1474–1489.

Desbois M, Kayiranga T, Gnamien B, Guessous S, Picon L. 1988. Characterization of some elements of the Sahelian climate and their interannual variations for July 1983, 1984 and 1985 from the analysis of Meteosat ISCCP data. *J. Climate* **1**: 867–904.

Dufresne J-L, Quaas J, Boucher O, Denvil S, Fairhead L. 2005. Contrasts in the effects on climate of anthropogenic sulfate aerosols between the 20th and the 21st century. *Geophys. Res. Lett.* **32**: L21703, DOI: 10.1029/2005GL023619.

Emanuel KA. 1991. A scheme for representing cumulus convection in large-scale models. *J. Atmos. Sci.* **48**: 2313–2335.

Fouquart Y, Bonnel B. 1980. Computations of solar heating on the Earth's atmosphere: a new parametrization. *Contrib. Atmos. Phys.* **53**: 35–62.

Grandpeix J-Y, Lafore J-P. 2010. A density current parameterization coupled with Emanuel's convection scheme. Part I: The models. *J. Atmos. Sci.* **67**: 881–897.

Guichard F, Petch JC, Redelsperger J-L, Bechtold P, Chaboureau J-P, Cheinet S, Grabowski W, Grenier H, Jones CG, Koehler M, Piriou J-M, Tailleux R, Tomasini M. 2004. Modelling the diurnal cycle of deep precipitating convection over land with cloud-resolving models and single-column models. *Q. J. R. Meteorol. Soc.* **130**: 3139–3172.

Hourdin F, Musat I, Bony S, Braconnot P, Codron F, Dufresne J-L, Fairhead L, Filiberti M-A, Friedlingstein P, Grandpeix J-Y, Krinner G, Le Van P, Li Z-X, Lott F. 2006. The LMDZ4 general circulation model: Climate performance and sensitivity to parametrized physics with emphasis on tropical convection. *Clim. Dyn.* **27**: 787–813.

Houze RA. 1997. Stratiform precipitation in regions of convection: A meteorological paradox? *Bull. Am. Meteorol. Soc.* **78**: 2179–2196.

Huffman GJ, Adler RF, Arkin P, Chang A, Ferraro R, Gruber A, Janowiak J, McNab A, Rudolf B, Schneider U. 1997. The Global Precipitation Climatology Project (GPCP) combined precipitation dataset. *Bull. Am. Meteorol. Soc.* **78**: 5–20.

Huffman GJ, Bolvin DT, Nelkin EJ, Wolff DB. 2007. The TRMM Multisatellite Precipitation Analysis (TMPA): Quasi-global, multiyear, combined-sensor precipitation estimates at fine scales. *J. Hydrometeorol.* **8**: 38–55.

Jenkins G, Kucera P, Joseph E, Fuentes J, Gaye A, Gerlach J, Roux F, Viltard N, Papazzoni M, Protat A, Bouniol D, Reynolds A, Arnault J, Badiane D, Kebe F, Camara M, Sall S, Ndiaye SA, Deme A. 2010. Coastal observations of weather features in Senegal during the African Monsoon Multidisciplinary Analysis Special Observing Period 3. *J. Geophys. Res.* **115**: D4132–4146, DOI: 10.1029/2009JD 013022.

Khairoutdinov M, Randall D. 2006. High-resolution simulation of shallow-to-deep convection transition over land. *J. Atmos. Sci.* **63**: 3421–3436.

Kummerow C, Hong Y, Olson WS, Yang S, Adler RF, McCollum J, Ferraro R, Petty G, Shin D-B, Wilheit TT. 2001. The evolution of the Goddard profiling algorithm (GPROF) for rainfall estimation from passive microwave sensors. *J. Appl. Meteorol.* **40**: 1801–1820.

Laing AG, Carbone R, Levizzani V, Tuttle J. 2008. The propagation and diurnal cycles of deep convection in northern tropical Africa. *Q. J. R. Meteorol. Soc.* **134**: 93–109.

Lemone MA. 1973. The structure and dynamics of horizontal roll vorticies in the planetary boundary layer. *J. Atmos. Sci.* **30**: 1077–1091.

Lima MA, Wilson JW. 2008. Convective storm initiation in a moist tropical environment. *Mon. Weather Rev.* **136**: 1847–1864.

Louis J-F. 1979. A parametric model of vertical eddy fluxes in the atmosphere. *Boundary-Layer Meteorol.* **17**: 187–202.

Mathon V, Laurent H. 2001. Life cycle of Sahelian mesoscale convective cloud systems. *Q. J. R. Meteorol. Soc.* **127**: 377–406.

Mohr KI. 2004. Interannual, monthly, and regional variability in the wet season diurnal cycle of precipitation in sub-Saharan Africa. *J. Climate* **17**: 2441–2453.

Morcrette J-J, Smith L, Fouquart Y. 1986. Pressure and temperature dependence of the absorption in longwave radiation parametrizations. *Contrib. Atmos. Phys.* **59**: 455–469.

Nesbitt SW, Zipser EJ. 2003. The diurnal cycle of rainfall and convective intensity according to three years of TRMM measurements. *J. Climate* **16**: 1456–1475.

Rickenbach T, Ferreira RN, Guy N, Williams E. 2009. Radar-observed squall line propagation and the diurnal cycle of convection in Niamey, Niger, during the 2006 African Monsoon and Multidisciplinary Analyses Intensive Observing Period. *J. Geophys. Res.* **114**: D03107, DOI:10.1029/2008JD010871.

Rio C, Hourdin F. 2008. A thermal plume model for the convective boundary layer: Representation of cumulus clouds. *J. Atmos. Sci.* **65**: 407–425.

Rio C, Hourdin F, Grandpeix J-Y, Lafore J-P. 2009. Shifting the diurnal cycle of parameterized deep convection over land. *Geophys. Res. Lett.* **36**: L07809, DOI: 10.1029/2008GL036779.

Roca R, Chambon P, Jobard I, Kirstetter P-E, Gosset M, Bergès J-C. 2010. Comparing satellite and surface rainfall products over West Africa at meteorologically relevant scales during the AMMA campaign using error estimates. *J. Appl. Meteorol. Clim.* **49**: 715–631.

Schumacher C, Houze RA, Jr. 2003. Stratiform rain in the Tropics as seen by the TRMM precipitation radar. *J. Climate* **16**: 1739–1756.

Shinoda M, Okatani T, Saloum M. 1999. Diurnal variations of rainfall over Niger in the West African Sahel: A comparison between wet and drought years. *Int. J. Climatol.* **19**: 81–94.

Sundqvist H. 1978. A parametrization scheme for non convective condensation including prediction of cloud water content. *Q. J. R. Meteorol. Soc.* **104**: 677–690, DOI: 10.1002/qj.49710444110.

Wallace JM. 1975. Diurnal variations in precipitation and thunderstorm frequency over the conterminous United States. *Mon. Weather Rev.* **103**: 406–419.

Williams M, Houze RA. 1987. Satellite-observed characteristics of winter monsoon cloud clusters. *Mon. Weather Rev.* **115**: 505–519.

Yamada T. 1983. Simulations of nocurnal drainage flows by a q^2l turbulence closure model. *J. Atmos. Sci.* **40**: 91–106.

Yang G-Y, Slingo J. 2001. The diurnal cycle in the Tropics. *Mon. Weather Rev.* **129**: 784–801.

Yang G-Y, Smith EA. 2008. Convective–stratiform precipitation variability at seasonal scale from 8 yr of TRMM observations: Implications for multiple modes of diurnal variability. *J. Climate* **21**: 4087–4114.

Yang S, Kuo K-S, Smith EA. 2008. Persistent nature of secondary diurnal modes of precipitation over oceanic and continental regimes. *J. Climate* **21**: 4115–4131.

